공학석사 학위논문

Fabrication of $CH_3NH_3SnI_3$ perovskite solar cells using vacuum process

진공 공정을 이용한 $CH_3NH_3SnI_3$ 페로브스카이트 태양전지의 제작

2016년 2월

서울대학교 대학원

재료공학부

최 민 형

Fabrication of $CH_3NH_3SnI_3$ perovskite solar cells using vacuum process

지도 교수 김 장 주

이 논문을 공학석사 학위논문으로 제출함

2016년 2월

서울대학교 대학원

재료공학부

최 민 형

최민형의 공학석사 학위논문을 인준함

2016년 2월

주 조 원 호 (인)

부 김 장 주 (인)

부 남 기 태 (인)

Abstract

Fabrication of $CH_3NH_3SnI_3$ perovskite solar cells using vacuum process

Choi Minhyung
Department of Materials Science and Engineering
The Graduate School
Seoul National University

Recently, hybrid organic-inorganic perovskite solar cells have attracted the great attention because of their remarkably high power conversion efficiency (*PCE*) combined with simple and low temperature process. But most of the devices reported up to now are Pb-based perovskite (e.g., $CH_3NH_3PbI_3$) solar cells which have potential risk such as heavy metal pollution, lead poisoning and lead accumulation. Therefore, replacing Pb in the perovskite is one of the most important issues in the field of perovskite solar cells for their commercialization and practical applications in the future. Until now, Sn has been considered the most viable element for replacing Pb in perovskite since Sn is the group 14 elements in periodic table and it is also known that Sn can adopt perovskite structure with $CH_3NH_3^+$ and I^-

ions. Based on this knowledge, some papers have reported lead-free Sn-based perovskite solar cells since 2014, however, all reported devices have been fabricated by spin-coating process. In the spin-coating process, electron transporting layer (ETL) under the perovskite is limited to mesoporous TiO_2 (mp-TiO_2) which causes poor surface morphology of $CH_3NH_3SnI_3$ perovskite film. Low stability to oxidation and short carrier diffusion lengths have been also pointed out as the critical problems for solution-processed $CH_3NH_3SnI_3$ perovskite. In this regard, vacuum process can be appropriate method for deposition of lead-free $CH_3NH_3SnI_3$ perovskite film because vacuum process has several advantages such as clean environment, wide selection of charge transporting layer and high reproducibility. The clean deposition condition in vacuum process is very effective to easily oxidizable $CH_3NH_3SnI_3$ film and various charge transporting layers can be chosen in consideration of better morphology of perovskite and well-matched energy level alignment.

In this work, various hole transporting layers (HTLs) are introduced and the effect of HTLs on the growth of vacuum-processed $CH_3NH_3SnI_3$ perovskite film is investigated. As a result, $CH_3NH_3SnI_3$ film shows the most improved crystallinity on ITO/MoO_3/NPB sublayer compared to on ITO and on ITO/MoO_3 sublayer. The initial growth of 2 nm-thick SnI_2 on each sublayer strongly affects total

growth of $CH_3NH_3SnI_3$, which is confirmed by X-ray diffraction (XRD) patterns. In addition, the effect of working pressure and thickness on the growth and film qualities of $CH_3NH_3SnI_3$ perovskite is investigated. Controlling the increase in working pressure by evaporated CH_3NH_3I, stoichiometric and unifrom $CH_3NH_3SnI_3$ perovskite film with nearly crystalline morphology is successfully formed at the apparent working pressure of 5×10^{-5} torr. The perovskite film fabricated at this pressure also shows the highest hole mobility due to the increased crystallinity and band gap energy of 1.33 eV. Lastly, optical simulation and fabrcating real $CH_3NH_3SnI_3$ perovskite solar cells are conducted. Although real lead-free device exhibits poor performance due to the lack of optimization, optical simulation results indicate that short-circuit current (J_{SC}) of the device can be increased up to ~23 mA/cm^2 when thickness of perovskite reaches around 500 nm. If open-circuit voltage (V_{OC}) reaches 0.88 V and fill factor (*FF*) attains ~0.7, the *PCE* of lead-free perovskite solar cells is expected to be ~14.2 % which is comparable to the Pb-based perovskite solar cells.

Keywords: Organic/inorganic hybrid perovskite solar cell, vacuum process, sublayer, $CH_3NH_3SnI_3$, lead-free perovskite, MoO_3, NPB

Student Number: 2014 – 21461

List of Tables

List of Figures

Chapter 1
Introduction

1.1 Motivation and outline of thesis

1.1.1 Motivation

Hybrid organic-inorganic perovskite solar cells have attracted the great attention due to their remarkably high power conversion efficiency (*PCE*) combined with simple and low temperature processes [16-20]. Compared to conventional organic solar cells, perovskite solar cells have been rapidly developed since 2009 and the *PCE* has reached ~20 % recently [4-5]. But most of the devices reported up to now is Pb-based perovskite (e.g., $CH_3NH_3PbI_3$) solar cells which can have potential side effects on environment and human body such as heavy metal pollution, lead poisoning and lead accumulation, etc. Thus replacing Pb in the perovskite is one of the most critical issues in the field of perovskite solar cells for their commercialization and practical applications in the future. In view of this, Sn is considered the most viable element for replacing Pb because Sn is the group 14 elements with the same ionic valency as Pb and Sn has the ionic radius of 69 pm

which is similar to that of Pb. In 2014, M. G. Kanatzidis and his coworker first reported lead-free Sn-based perovskite solar cells fabricated by spin-coating process and the device exhibited the efficiency of 5.48 % [7]. However, methylammonium tin iodide ($CH_3NH_3SnI_3$) perovskite film on mesoporous titanium dioxide (mp-TiO_2) used as electron transporting layer (ETL) in the device showed rough surface morphology with many pin-holes in this report. After that, H. J. Snaith and his coworker has also reported $CH_3NH_3SnI_3$ perovskite solar cells and the *PCE* has improved up to 6.4 %, however, stability of $CH_3NH_3SnI_3$ to oxidation and short carrier diffusion lengths were pointed out as the severe problems for solution-processed lead-free perovskite film [8].

Vacuum process can be appropriate way to fabricate efficient lead-free $CH_3NH_3SnI_3$ perovskite solar cells because vacuum process has several advantages such as clean environment, wide selection of charge transporting layer and high reproducibility [22-24]. The clean deposition condition in vacuum process is very effective to easily oxidizable $CH_3NH_3SnI_3$ film. In addition, various charge transporting layer, so-called sublayer because it is located under the perovskite layer, can be chosen in consideration of better morphology of perovskite and well-matched alignment of energy level. Furthermore, precise controls of deposition rate and working pressure in the chamber are possible in

vacuum process resulting in uniform and stoichiometric perovskite film with high reproducibility. In this thesis paper, characterization of $CH_3NH_3SnI_3$ perovskite film fabricated in vacuum process will be conducted through X-ray diffraction (XRD), scanning electron microscopy (SEM), energy-dispersive X-ray spectroscopy (EDS), atomic force microscopy (AFM) and optical absorption measurement, etc. The effect of sublayer under the perovskite, working pressure and film thickness on the growth of perovskite in vacuum process will be precisely investigated. Optical simulation and real performance of lead-free perovskite solar cells will be also measured and discussed in the final stage.

1.1.2 Outline of thesis

In chapter 1, the brief introduction of the perovskite materials and operation principles of perovskite solar cells will be described. Short explanation for appearance of Sn-based perovskite solar device and fabricating $CH_3NH_3SnI_3$ film in vacuum process will be also included in this chapter..

In chapter 2, the effect of hole transporting layers (HTLs) under the perovskite on the growth of $CH_3NH_3SnI_3$ film will be investigated by using X-ray diffraction (XRD). In addition, experimental details for

depositing perovskite in vacuum process are concretely described and the reason why crystallinity of $CH_3NH_3SnI_3$ differs depending on each sublayer will be discussed.

In chapter 3, composition of $CH_3NH_3SnI_3$ perovskite film will be controlled by the increase in apparent working pressure resulting from evaporated CH_3NH_3I. The effect of this working pressure on elemental composition and total growth of the $CH_3NH_3SnI_3$ film will be investigated using several spectroscopes and other measurements. In addition, electrical properties of stoichiometric $CH_3NH_3SnI_3$ film which shows nearly crystalline morphology will be analyzed.

In chapter 4, the influence of film thickness on the properties of $CH_3NH_3SnI_3$ perovskite film will be investigated. Change of crystallinity in perovskite film with thickness and elemental composition of overall $CH_3NH_3SnI_3$ film will be analyzed by using XRD and cross-sectional energy-dispersive X-ray spectroscopy (EDS) measurement, respectively.

In chapter 5, refractive index of stoichiometric $CH_3NH_3SnI_3$ film is obtained by ellipsometry and transfer matrix method. Optical simulation of lead-free $CH_3NH_3SnI_3$ perovskite solar cells will be conducted using these optical constants. In addition, the maximum PCE of lead-free perovskite solar cells will be predicted and fabrication of real lead-free device in vacuum process will be done based on the

optical simulation results.

1.2 Perovskite solar cells

1.2.1 Material properties of perovskite

Perovskite is a type of crystal structure with chemical formula of ABX_3. In perovskite solar cells, organometal halide perovskite is most commonly used as absorber materials where A is $CH_3NH_3^+$, B is Pb^{2+} or Sn^{2+}, and X is I^- although there are a few reported papers that use $HC(NH_2)_2^+$ [25-26], Cs^+ [27-29] and mixed halide [30]. In case of mostly used $CH_3NH_3PbI_3$, this perovskite has optical band gap of 1.5 eV and shows high absorption coefficient in the visible light range. In addition, several papers have reported that diffusion lengths of electrons and holes are up to 1 micrometer in $CH_3NH_3PbI_3$, which is probably due to the shallow traps against electronic band edge of perovskite. Furthermore, $CH_3NH_3PbI_3$, perovskite has other unique properties such as ambipolar charge transport, low exciton binding energy, and easily tunable electronic band gap. These characteristics make it well suited for photovoltaic (PV) devices, light-emitting diodes

(LEDs), and even lasers.

In case of $CH_3NH_3SnI_3$, this material adopts perovskite structure crystallizing in the pseudocubic space group *P*4*mm* in any conditions with lattice parameters of $a = b = 6.240$ Å and $c = 6.281$ Å [21]. Also, $[SnI_6]^{4-}$ polyhedra in all perovskite lattice make an infinite 3D lattice structure with Sn–I–Sn connecting angles of ~177.4° and 180° along the a- and c-axes [6].

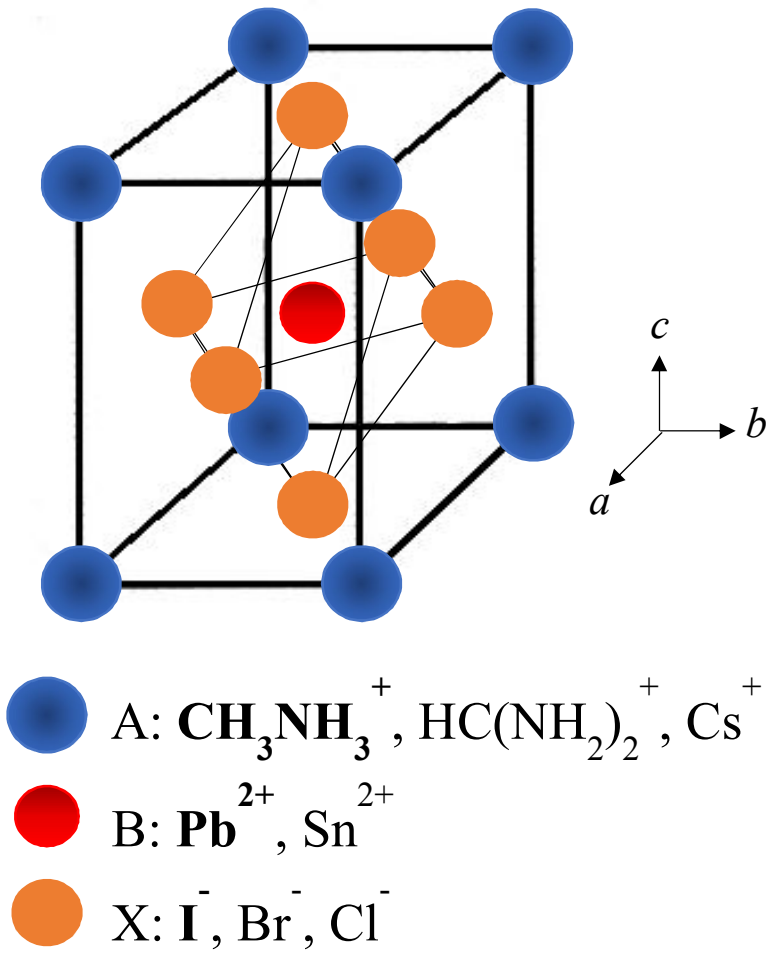

Figure. 1.1 The structure of organometal halide perovskite consisting of A cations located at tetragonal edge (thick lines) and corner-sharing BX_6^{4-} octahedron (drawn with thin lines). The bold marks in the parentheses are most widely used components which are $CH_3NH_3^+$, Pb^{2+} and I^-, respectively.

1.2.2 Operating principles of perovskite solar cells

$CH_3NH_3PbI_3$ perovskite has a very low exciton binding energy about 20-50 meV which is comparable to the room temperature thermal energies of k_BT ~ 25 meV. Recently, several papers have suggested that free carriers are dominantly generated in the $CH_3NH_3PbI_3$ perovskite at room temperature which is calculated by thermodynamic simulation and optical density [1-2]. Therefore, generation of free carriers is mainly considered in perovskite solar cells.

After the free carriers are generated in perovskite active layer, they diffuse to charge transport layer benefiting from excellent electrical properties of perovskite. L. M. Herz and H. J. Snaith found that both monomolecular and bimolecular charge carrier recombination rates are extremely low with using transient THz spectroscopy [3]. They also have proposed the lower bound limits of charge carrier mobilities in perovskite is ~8 $cm^2\ V^{-1}\ s^{-1}$ which is several orders larger than the value of common conjugated organic molecules. These low recombination rates and large carrier mobility ensure long carrier diffusion length and charge carrier can be effectively extracted from perovskite layer and collected at the electrodes.

1.2.3 Lead-free perovskite solar cells

After Kojima et al. has first reported organic-inorganic lead halide perovskite solar cells, the power conversion efficiency (*PCE*) of Pb-based perovskite solar cells has been rapidly improved and reached ~20 % recently [4-5]. In addition to this prompt advance, low-cost and abundant starting materials, simple processing and its flexibility make Pb-based perovskite solar cells promising alternative to silicon solar cells.

However, one emerging concern is the toxicity of Pb in the perovskite solar cells. It is widely known that Pb causes severe heavy metal pollution to environment and critical lead accumulation to human being. Therefore, one of the most important issues in perovskite solar cells is to replace the Pb by another element which has less toxicity. In this regard, Sn has been nominated as the most viable element for replacing Pb in perovskite since Sn is the group 14 elements in periodic table and it is known that Sn can also adopt perovskite structure with $CH_3NH_3^+$ and I^- ions [6]. In 2014, M. G. Kanatzidis and his coworker first reported lead-free perovskite solar cells using mesoporous TiO_2 (mp-TiO_2) as electron transporting layer (ETL). The device showed notable *PCE* of ~5.7 %, however, solution-processed $CH_3NH_3SnI_3$ film on mp-TiO_2 exhibited poor film coverage with several pinholes [7]. Soon after, H. J. Snaith and his coworker reported another lead-free $CH_3NH_3SnI_3$

solar cells whose efficiency increased up to ~6.4 % and argued that Sn^{4+} generated by oxidation of Sn^{2+} acts as a p-type dopant and makes $CH_3NH_3SnI_3$ p-type semiconductors, which increases background hole concentration and results in significant carrier recombination [32]. Furthermore, charge carrier diffusion length was found to be ~30 nm in the solution-processed $CH_3NH_3SnI_3$ perovskite by using transient THz spectroscopy [8]. This poor electrical property might be factor to limit the performance of lead-free perovskite solar cells. M. G. Kanatzidis group has recently elucidated the solvent effect on crystallization of $CH_3NH_3SnI_3$ film and short-circuit current (J_{SC}) of lead-free device increased up to ~ 21 mA cm^{-2} with uniform perovskite film on mp-TiO_2 layer by using dimethyl sulfoxide (DMSO) as solvent [9].

1.2.4 Fabrication of $CH_3NH_3SnI_3$ thin film in vacuum process

$CH_3NH_3PbI_3$ (or $CH_3NH_3SnI_3$) is easily formed by the reaction between CH_3NH_3I (Methylammonium Iodide, MAI) and PbI_2 (or SnI_2). Most of processes for fabricating perovskite thin films are based on spin-coating process because of its ease and simplicity. In this process, the solvent should be resolving both CH_3NH_3I and PbI_2 (or SnI_2). Dimethylformamide (DMF) is widely used as solvent for spin-coating of perovskite, however, transporting layers are generally limited in this process due to the solubility of transporting layer under the perovskite.

Also, reproducibility of device, poor morphology of perovskite film and need for additional annealing process are often regarded as drawback in solution process.

To solve the problem mentioned above, some groups reported the vacuum deposition of perovskite layer for the solar cell [23]. In this process, MAI and the metal iodide (PbI_2 or SnI_2) are co-evaporated in the vacuum chamber and the composition is controlled by the amount of each source deposited. Vacuum deposition has several advantages such as clean environment, high reproducibility, wide choice of materials and usefulness for mass production [22-24]. There are notable things to fabricate perovskite thin films in vacuum process as follows.

Unusual behavior of CH_3NH_3I in the vacuum deposition

Typical thermal evaporating materials do not cause the increase in working pressure in vacuum chamber because the ejected molecules from the source adsorb on the substrates or the any part of the chamber rather than exist in the gaseous state. When CH_3NH_3I is evaporated in the vacuum chamber, however, the CH_3NH_3I source are randomly distributed in the chamber and it behaves as gaseous species causing the increase in the working pressure infiltrating to the ion gauge. This behavior is probably resulting from the low molecular weight of CH_3NH_3I (157 g/mol), low evaporation temperature (~150℃) and low

stacking properties. Due to these characteristics when the CH_3NH_3I is only deposited onto the glass substrate, it is difficult to measure the exact thickness since the CH_3NH_3I is hardly adsorbed on the substrate. It is also considered that evaporated CH_3NH_3I is rarely stuck to gold (Au) substrate, that is, the quartz crystal microbalances (QCMs) which read the deposition rate of CH_3NH_3I by detecting the mass of evaporated materials adsorbed on them. In other words, controlling the amount of deposited CH_3NH_3I by using the only QCM may be inaccurate and unreliable. Therefore, it is reasonable for deposition amount of evaporated CH_3NH_3I to be controlled not by using QCM but by the increase in working pressure of vacuum chamber.

Co-evaporation of CH_3NH_3I and SnI_2

Figure 1.2. shows the schematic description of experimental set-up for co-evaporating CH_3NH_3I and SnI_2 in the vacuum chamber. The triiodide tin perovskite, $CH_3NH_3SnI_3$, is easily formed with the reaction between the evaporated CH_3NH_3I and evaporated SnI_2. As shown in figure 1.2, the quartz crystal microbalances 1 (QCM) was located on the SnI_2 source which reads only the deposition rate of SnI_2. The QCM 1 was enclosed by the aluminum foil to exclude the effect of the CH_3NH_3I, due to its gas-like behavior in the vacuum chamber. In this co-evaporation process, the deposition rate of SnI_2 was firstly reached

to the steady state. And then, QCM 2 located at the near the substrate which enables to read the deposition rate of CH_3NH_3I and also the thickness of the perovskite reads the rate of both SnI_2 and CH_3NH_3I which forms the Sn perovskite on the substrate. The base pressure of the vacuum chamber was about 1×10^{-6} torr and this pressure was increased up to 1×10^{-5} torr when CH_3NH_3I starts to be evaporated. Although the deposition rates of the SnI_2 and CH_3NH_3I are maintained constant during the co-deposition, molar ratio of deposited CH_3NH_3I and SnI_2 is controlled by not the rate but the increase in apparent working pressure for the reason described in the prior section. In addition, the 'working pressure' in this paper means the pressure detected by ion gauge and indicated on the controller. To be exact, this pressure should be called 'apparent working pressure' since ion gauge in vacuum chamber is adjusted to the air gas, however, two terms will be used interchangeably in this paper for convenience sake.

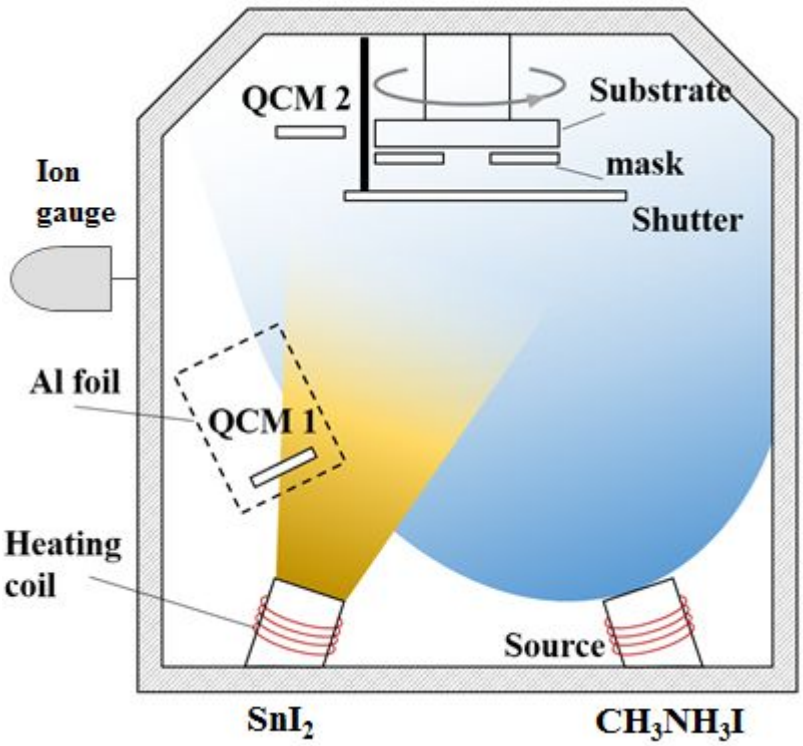

Figure 1.2. The schematic description of co-evaporating CH_3NH_3I and SnI_2 in the vacuum chamber.

Chapter 2

The effect of HTLs on formation and growth of $CH_3NH_3SnI_3$ perovskite film

2.1 Introduction

One of the most important issues in perovskite solar cells is to grow perovskite film which is nearly single crystalline. It has been reported that optical and electrical properties such as absorption, carrier diffusion length and surface quality are dramatically improved in single crystal perovskite [31], which is essential for accomplishing high device performance. In order to epitaxially grow single crystalline perovskite film, pre-depositing suitable sublayer under the active layer is significant with regard to lattice structure as well as energy level. A. Amassian and his coworker reported that $CH_3NH_3PbI_3$ perovskite film has more dense interface on copper(I) thiocyanate (CuSCN) than on poly(3,4-ethylenedioxythiophene) : poly(styrenesulfonate) (PEDOT : PSS) [10] by using scanning electron spectroscopy (SEM) image. In addition, Alex K. Y. Jen and his coworker suggested that $CH_3NH_3PbI_3$ perovskite film has similar morphology on both ITO and PEDOT : PSS layers, and they successfully fabricated hole-transporting layer-free

perovskite solar cell . However, it is still a unresolved question which sublayer results in the best surface morphology of lead-free $CH_3NH_3SnI_3$ perovskite film and increases the crystallinity. Therefore, the crystallinity of $CH_3NH_3SnI_3$ perovskite film on the various sublayers will be investigated by using X-ray diffraction (XRD) measurement in this chapter.

2.2 Experiments

150 nm-thick ITO coated glass substrates were successfully cleaned with acetone and isopropyl alcohol (IPA) solution. All of the materials except $CH_3NH_3SnI_3$ perovskite were thermally heated and evaporated at the base pressure of $<1\times10^{-6}$ torr in the chamber. When CH_3NH_3I (Jida Ruibo Optoelectronics Tech.) is thermally evaporated in the chamber, the apparent working pressure was raised up to 1×10^{-5} torr which is similar to the previous reports [23,24].

The deposition rate of CH_3NH_3I was monitored in real time using a crystal thickness sensor (INFICON, 5MHz) with simultaneously checking the working pressure of the chamber by ion gauge. The deposition rate of SnI_2 (Alpha Aesar) was kept constant during the co-deposition. The perovskite layer was deposited in vacuum chamber without annealing process and the details about co-deposition process

for perovskite are deliberately described in chapter 1.2.4. The MoO_3 (Sigma Aldrich) and the BCP (Nichem) layers were deposited at a rate of 0.2 Å/s. The NPB (Nichem) and the C_{60} (SES Research) layers were deposited at a rate of 1 Å/s. The BCP (Nichem) and the Al layers were deposited at a rate of 0.5 Å/s and 4 Å/s respectively. The deposition rates were calibrated using a profilometry (KLA-Tencor Alpha-Step IQ) before depositing each material. The active area of each device was 4 mm^2 and 72 devices could be fabricated to the max. After finishing all the evaporation, the devices were encapsulated using an epoxy resin with glass cans in an N2 environment. The UV-vis absorption spectra of the films were recorded with a VARIAN Cary 5000 UV-vis spectrophotometer. The current density-voltage (J–V) characteristics were measured under simulated AM 1.5G sunlight of 100 mW/cm^2 using Newport (91160A) solar simulator, and recorded using a Keithley 237 source measurement unit at room temperature. The light intensity was calibrated using a standard Si-solar cell (NREL). The scan step of J-V characteristics was 0.02 V with 0.3 seconds of interval time for each step, and the scan direction was from negative to positive voltage. The incident photon to electron conversion efficiency (IPCE) was measured using a 1000 W Xe lamp combined with a monochromator and its intensity was calibrated with a Si photodiode. The IPCE was measured without light bias under the short circuit condition. The

atomic force microscopy (AFM) image was taken by PSIA XE-100 scanning probe microscope in noncontact mode

2.3 Results and discussion

Figure 2.1 shows the XRD pattern of $CH_3NH_3SnI_3$ perovskite film grown on 150 nm-thick ITO substrate at different working pressures. All $CH_3NH_3SnI_3$ films deposited on ITO substrate exhibit sharp (110) peak which corresponds to the reported one. But peak intensity of $CH_3NH_3SnI_3$ film on ITO is somewhat low indicating that perovskite has poor crystallinity on the substrate.

To obtain better crystalline perovskite film, MoO_3 (5 nm) and MoO_3 (5 nm)/NPB (20 nm) sublayers under the perovskite are deposited on ITO. Both layers are widely used as hole transporting layers (HTLs) in the field of organic solar cells [33-34]. Figure 2.2 (a) shows the XRD pattern and absorbance of $CH_3NH_3SnI_3$ perovskite films deposited on different sublayers. It seems that $CH_3NH_3SnI_3$ perovskite is rarely formed on MoO_3 sublayer. It should be noted that $CH_3NH_3SnI_3$ film fabricated on MoO_3/NPB layer shows extremely strong and sharp (100) and (200) peaks in XRD pattern, which means that the crystallinity of perovskite film amazingly increases on MoO_3/NPB sublayer. In addition, absorption of perovskite film is the highest on the MoO_3/NPB

sublayer as shown in figure 2.2 (b), which is consistent with increased crystallinity of $CH_3NH_3SnI_3$ film. To figure out the reason for different crystallinity of perovskite film on each sublayer, XRD pattern of 50 nm-thick SnI_2 film is measured. Interestingly, tendency of XRD pattern for SnI_2 film is in accordance with that for $CH_3NH_3SnI_3$ film depending on sublayers. This indicates that initial growth of 2 nm-thick SnI_2 on each sublayer strongly affects the total growth of $CH_3NH_3SnI_3$ film.

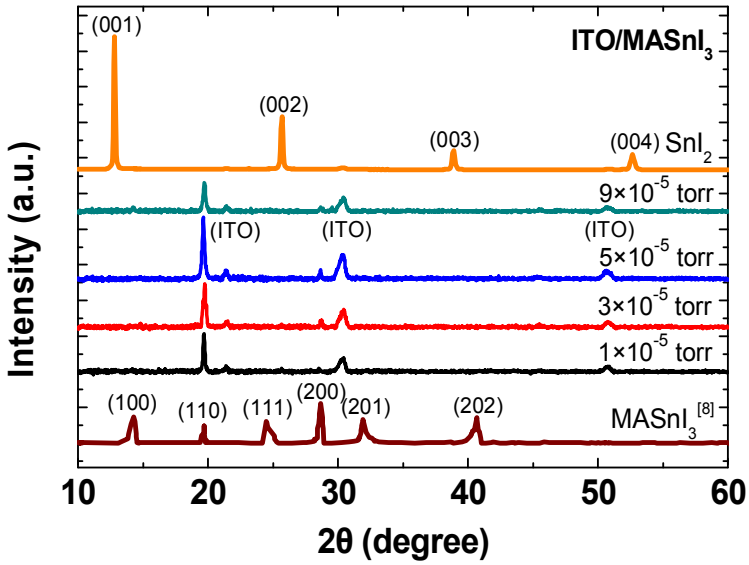

Figure 2.1. The X-ray diffraction (XRD) patterns $CH_3NH_3SnI_3$ films deposited on 150 nm-thick ITO at different working pressures. Thickness of perovskite films is 46 nm, 52 nm, 66 nm and 70 nm at 1×10^{-5} torr, 3×10^{-5} torr, 5×10^{-5} torr and 9×10^{-5} torr, respectively. Reported XRD pattern with peak index is powder XRD. Peak intensities of $CH_3NH_3SnI_3$ films and SnI_2 film are enlarged and reduced by 2.5 times, respectively.

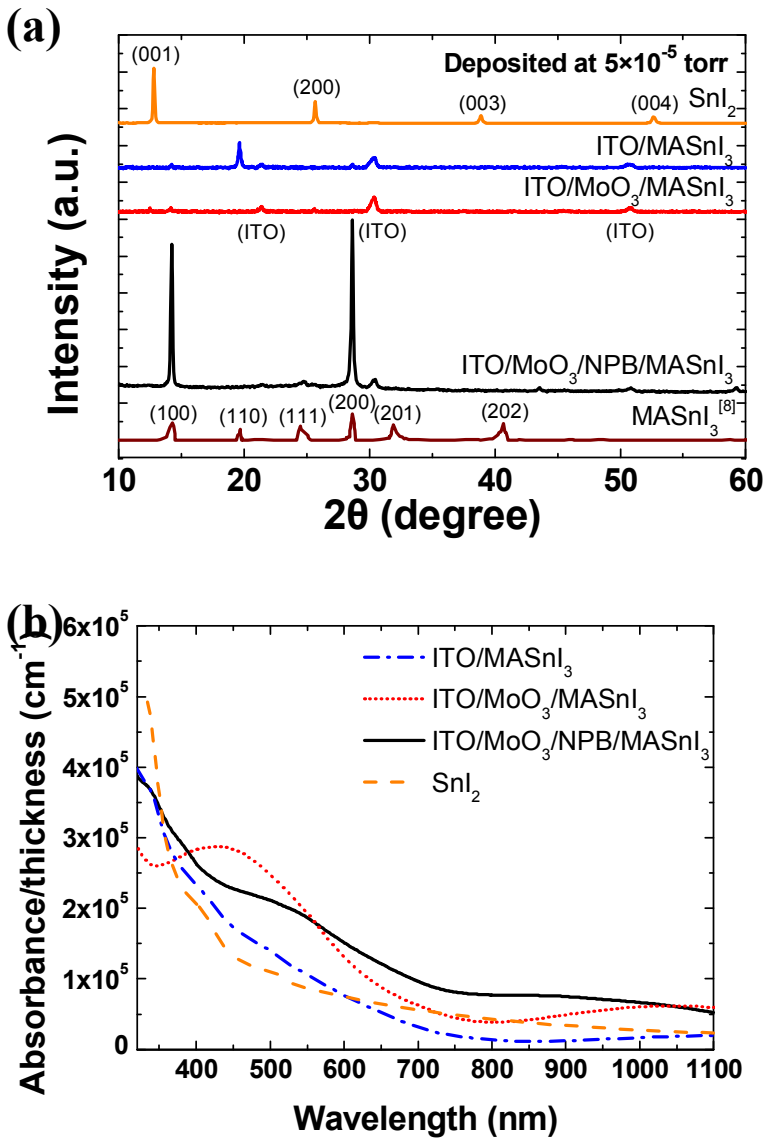

Figure 2.2. (a) The X-ray diffraction (XRD) patterns and (b) absorbance of $CH_3NH_3SnI_3$ films deposited on ITO (150 nm), ITO (150 nm)/MoO_3 (5 nm) and ITO (150 nm)/MoO_3 (5 nm)/NPB (20 nm) sublayers. XRD peak intensities of $CH_3NH_3SnI_3$ films and SnI_2 film are enlarged and reduced by 2.5 times, respectively.

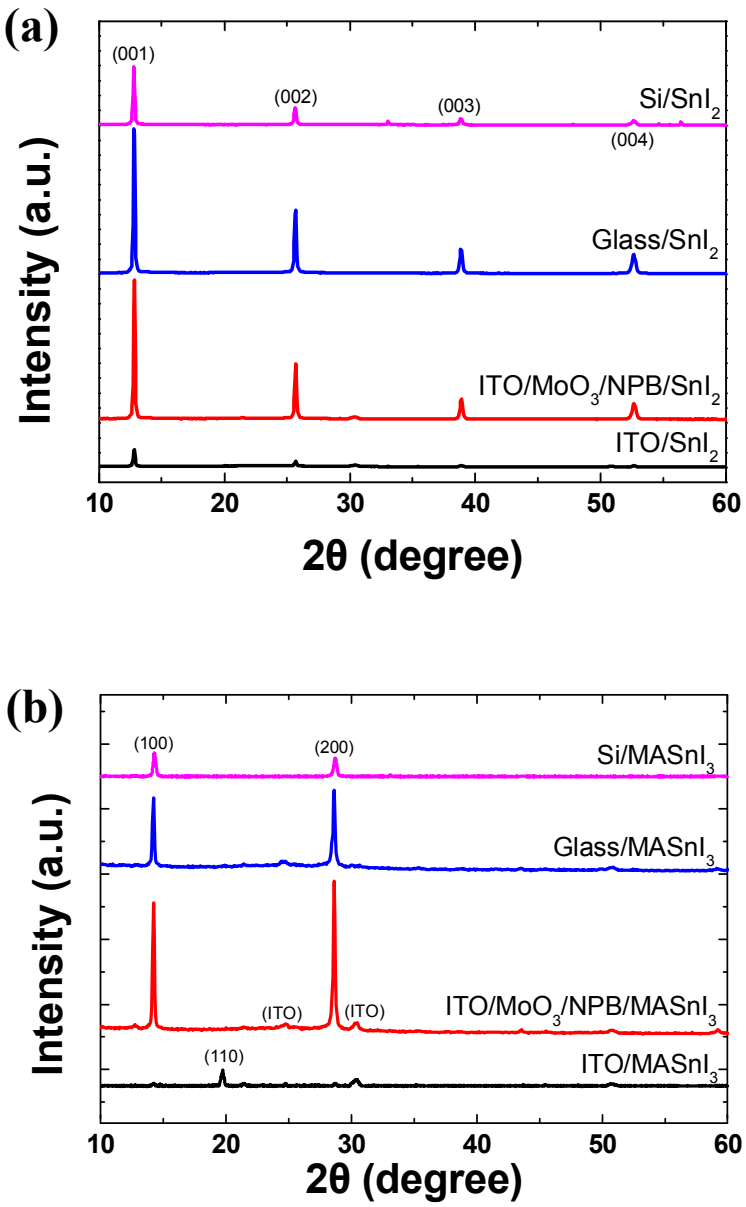

Figure 2.3. (a) The X-ray diffraction (XRD) patterns of 50 nm-thick SnI_2 films deposited on different sublayers and (b) The X-ray diffraction (XRD) patterns of 50 nm-thick $CH_3NH_3SnI_3$ films on the various sublayers.

2.4 Conclusion

In this chapter, the effect of sub-HTLs on the formation of $CH_3NH_3SnI_3$ perovskite is investigated. The XRD results show that $CH_3NH_3SnI_3$ perovskite is difficult to be formed on ITO (150 nm)/MoO_3 (5 nm) layer and has a poor crystallinity on ITO (150 nm) substrate. But crystallinity of perovskite film is extremely improved when deposited on ITO (150 nm)/MoO_3 (5 nm)/NPB (20 nm) layer. This increased crystallinity implies better electrical and optical properties of perovskite film and is essential for enhancing device performance. The reason why $CH_3NH_3SnI_3$ perovskite film has the highest crystallinity on ITO/MoO_3/NPB layer is probably related to initial 2 nm-thick crystalline SnI_2 film. This interesting result can be applied to vacuum-processed $CH_3NH_3PbI_3$ perovskite solar cells to obtain better lead perovskite film as well as lead-free perovskite solar cells.

Chapter 3

The effect of working pressure on composition and growth of $CH_3NH_3SnI_3$ perovskite film

3.1 Introduction

The control of elemental composition of perovskite film is another critical factor to determine growth of perovskite [11]. N. G. Park and his coworker reported that concentraion of CH_3NH_3I solution in two-step spin-coating process strongly affects the crsytal growth of $CH_3NH_3PbI_3$ and hold sway in final cuboid size of the perovskite film [12]. They found that higher CH_3NH_3I concentration resulted in the smaller cuboid size of perovskite because the growth of seed crystal was easily inhibited by other neibouring seed crystals at the higher concentration. Also, several reports suggest that composition of perovskite in solution process significantly influences reaction kinetics, absorption, stability and surface morphology of perovskite film which are closely related to the overall device performance [11-14]. Elemental composition of perovskite film can be directly controlled by concentration of initial CH_3NH_3I (or metal iodide) solution in solution process. In vacuum process, composition of perovskite film can be

more easily and delicately controlled by depositon rate of CH_3NH_3I and metal iodide. But as described in chapter 1, CH_3NH_3I has a poor sticking property and this material may be difficult to be adsorbed to crystal thickness sensor causing reliability problem in deposition rate displayed on the controller. Therefore, we controlled the elemental composition of $CH_3NH_3SnI_3$ film via the increase in apparent working pressure by evaporated CH_3NH_3I and the detailed explanation can be found in chapter 1.1.4.

3.2 XRD and absorption spectrum

Figure 3.1 (a) shows the XRD patterns of $CH_3NH_3SnI_3$ perovskite films deposited on ITO (150 nm)/MoO_3 (5 nm)/NPB (20 nm) at the different working pressures. It should be noted that (100) and (200) peak intensities become maximum when perovskite is deposited at 5×10^{-5} torr, which means the crystallinity of perovskite film gets most improved at this condition. In addition, XRD patterns of the samples fabricated at 1×10^{-5} torr and 3×10^{-5} torr show (100) peak of SnI_2. This means that some amount of SnI_2 material is unreacted with CH_3NH_3I because the amount of evaporated CH_3NH_3I is insufficient in these working pressures. Therefore, it can be deduced that working pressure of 5×10^{-5} torr is the optimal condition for formation of growth

$CH_3NH_3SnI_3$ perovskite film whose composition is nearly ideal ratio of CH_3NH_3I and SnI_2. Real

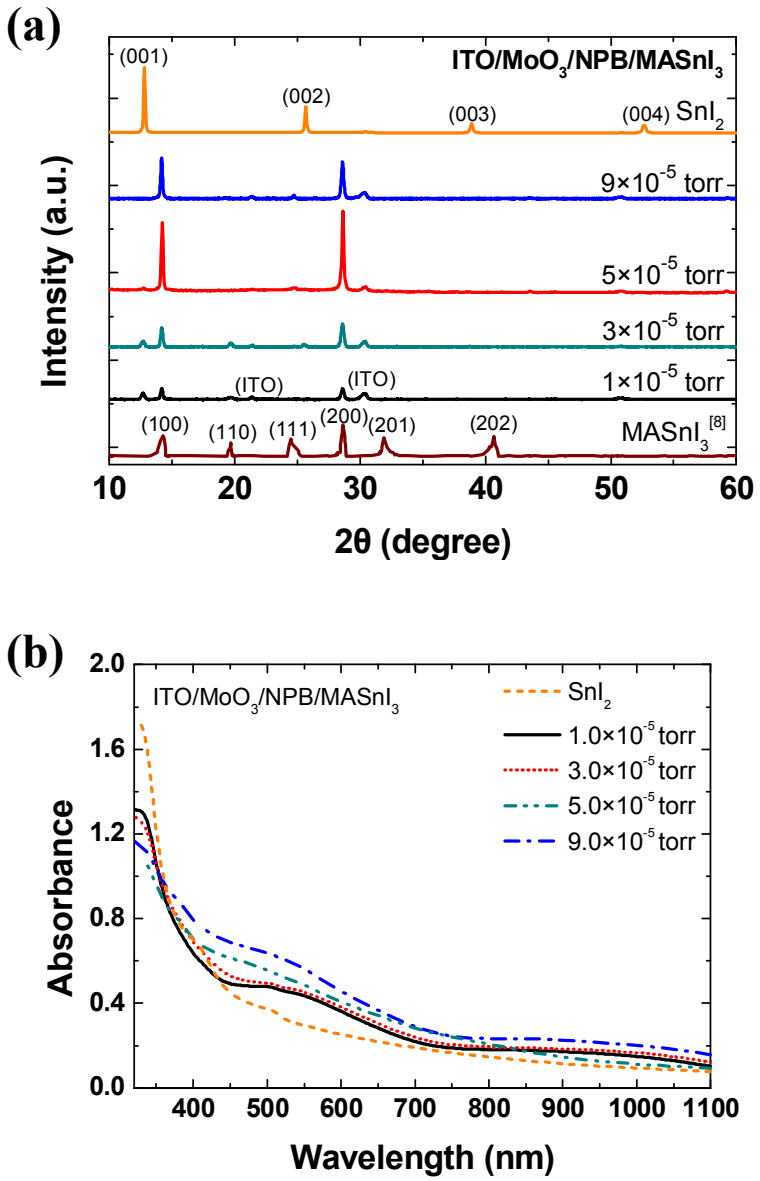

Figure 3.1. (a) XRD patterns and (b) absorbance of $CH_3NH_3SnI_3$ films deposited on ITO (150 nm)/MoO_3 (5 nm)/NPB (20 nm) at different working pressures. Thickness of perovskite films is 46 nm, 52 nm, 66 nm and 70 nm at 1×10^{-5} torr, 3×10^{-5} torr, 5×10^{-5} torr and 9×10^{-5} torr, respectively. Peak intensity of SnI_2 film is reduced by 2.5 times in

composition of $CH_3NH_3SnI_3$ perovskite film on ITO/MoO_3/NPB will be precisely investigated in chapter 3.4. By using the XRD results, crystalline sizes of all perovskite samples are also calculated from Scherrer equation as shown in Table 3.1. This equation is described as

$$\tau = \frac{K\lambda}{\beta \cos\theta} \tag{3.1}$$

Where K is a dimensionless shape factor which is typically 0.9, λ is the wavelength of X-ray, β is the full width at half maximum (FWHM) in radians and θ is the Bragg angle. The calculation result indicates that crystalline size of perovskite is the largest at 5×10^{-5} torr. These results can be rationalized by the hypothesis that compositional ratio of CH_3NH_3I and SnI_2 is so close to 1:1 at this pressure that formation and growth of $CH_3NH_3SnI_3$ perovskite are optimized and with little hindrance by unreacted CH_3NH_3I or SnI_2. Absorbance of $CH_3NH_3SnI_3$ perovskite films fabricated on ITO (150 nm)/MoO_3 (5 nm)/NPB (20 nm) at different pressures is also shown in figure 3.1 (b). Interestingly, absorbance of $CH_3NH_3SnI_3$ films gets increased as working pressure gets higher in the wavelength range of around 400-800 nm. This increase is in accordance with the increase in thickness of perovskite samples, which is probably because the amount of deposited CH_3NH_3I increases. The deposited CH_3NH_3I cannot be detected by XRD due to the small molecular amorphous characteristics of the

material, however, it has a kind of absorption in the visible light rage.

Pressure	1×10^{-5} torr		3×10^{-5} torr		5×10^{-5} torr		9×10^{-5} torr	
Grain	(100)	(200)	(100)	(200)	(100)	(200)	(100)	(200)
Grain size	39.4 nm	30.6 nm	36.4 nm	31.5 nm	48.0 nm	39.9 nm	44.2 nm	38.9 nm

Table 3.1 Crystalline size of $CH_3NH_3SnI_3$ films deposited on ITO (150 nm)/MoO_3 (5 nm)/NPB (20 nm) at different working pressures calculated from Scherrer equation using XRD pattern in figure 3.1 (a).

3.3 Morphology of perovskite film

As discussed in chapter 3.2, crystallinity of $CH_3NH_3SnI_3$ perovskite films on ITO (150 nm)/MoO_3 (5 nm)/NPB (20 nm) varies with working pressures. Figure 3.2 shows the scanning electron microscopy (SEM) image of perovskite films fabricated on ITO/MoO_3/NPB layer at different pressures. As working pressure by evaporated CH_3NH_3I goes up from 1×10^{-5} torr to 5×10^{-5} torr, larger size of particles emerge which is consistent with the tendency of XRD patterns in figure 3.1 (a). In case of sample fabricated at 9×10^{-5} torr, size of particles hardly changes compared to the one at 5×10^{-5} torr. Also, the sample shows very rough surface morphology and there are several pinholes on the films which can cause current leakage and severe short-circuiting of the real device. Figure 3.3 shows atomic force microscopy (AFM) image of the same samples as shown in figure 3.2. Every AFM image takes after the SEM image and it should be noted that root mean square roughness (RMS roughness, Rq) becomes 3 times larger at 9×10^{-5} torr than 5×10^{-5} torr. This poor morphology means growth of compact and uniform perovskite film at the pressure of 9×10^{-5} torr is retarded by excessive CH_3NH_3I. In other words, $CH_3NH_3SnI_3$ films grown at 5×10^{-5} torr shows the most compact morphology which is nearly crystalline and this film is expected to exhibit improved structural and electrical

properties.

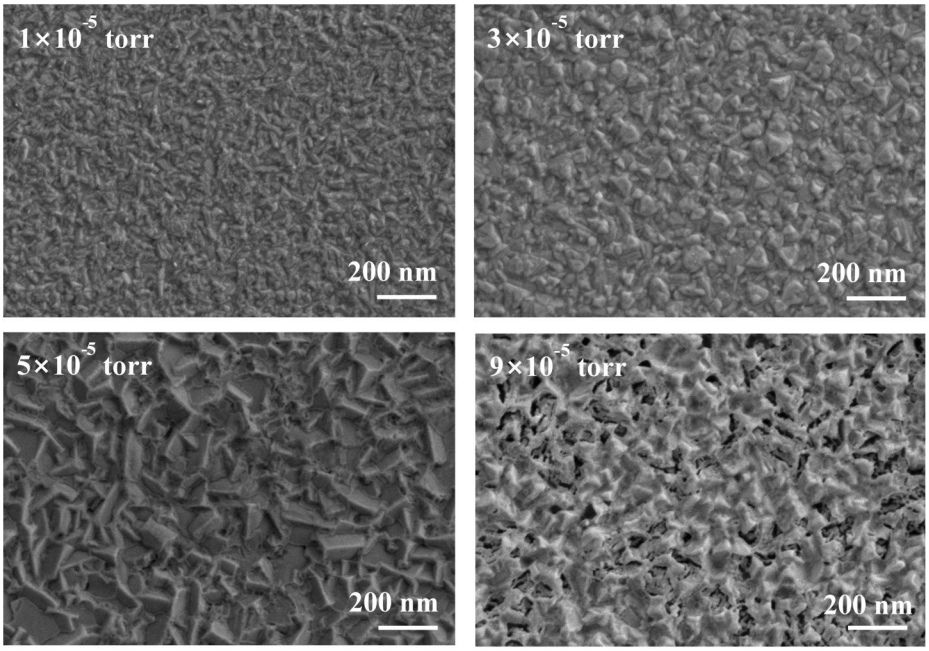

Figure 3.2. The scanning electron microscopy (SEM) image of $CH_3NH_3SnI_3$ films on ITO (150 nm)/MoO_3 (5 nm)/NPB (20 nm) deposited at different pressures. Thickness of perovskite films is 122 nm, 143 nm, 180 nm and 198 nm at 1×10^{-5} torr, 3×10^{-5} torr, 5×10^{-5} torr and 9×10^{-5} torr, respectively.

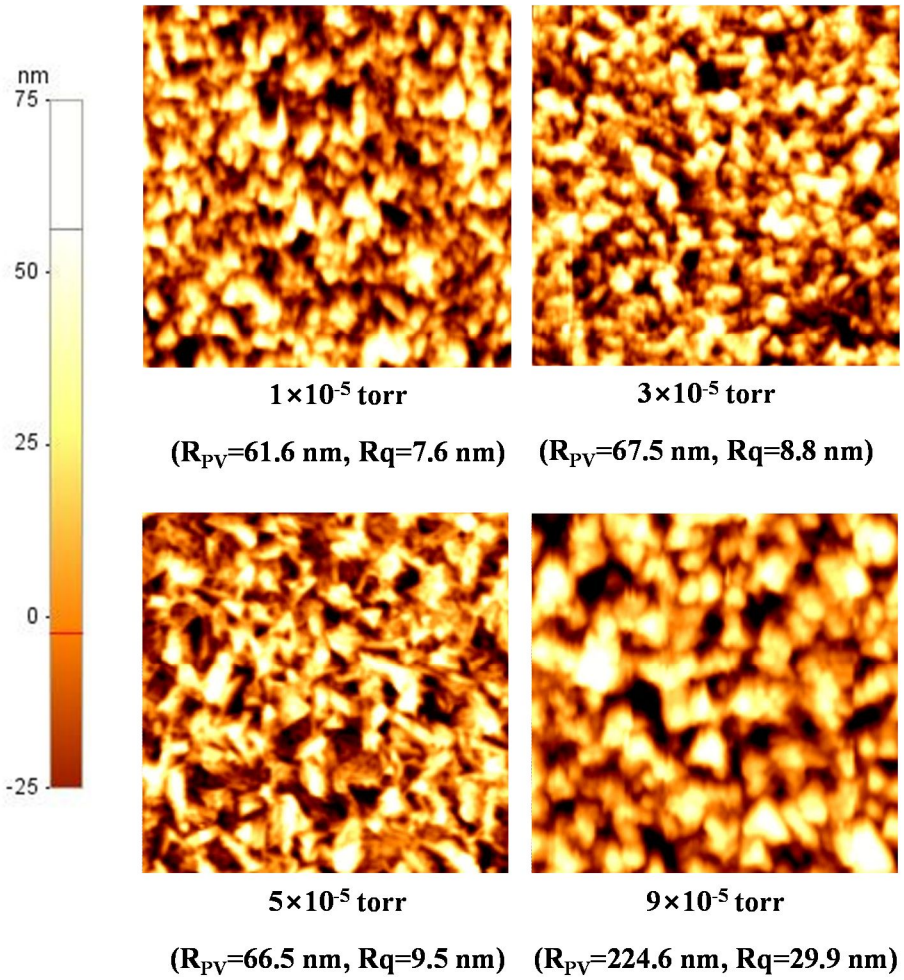

Figure 3.3. The atomic force microscopy (AFM) image of $CH_3NH_3SnI_3$ films on ITO (150 nm)/MoO_3 (5 nm)/NPB (20 nm) deposited at different pressures. Size of each image is 2 ㎛ × 2 ㎛. Thickness of perovskite films is 122 nm, 143 nm, 180 nm and 198 nm at 1×10^{-5} torr, 3×10^{-5} torr, 5×10^{-5} torr and 9×10^{-5} torr, respectively.

3.4 Elemental composition of perovskite film

Figure 3.4 shows energy-dispersive X-ray spectroscopy (EDS) result of $CH_3NH_3SnI_3$ perovskite films on ITO (150 nm)/MoO_3 (5 nm)/NPB (20 nm) at different working pressures. The most notable thing is that elemental composition of Sn and I is almost close to 1:3 in the sample fabricated at 5×10^{-5} torr where nearly crystalline morphology appears as discussed in the previous chapter. This indicates that the apparent working pressure of 5×10^{-5} torr is the optimal condition for formation and growth of $CH_3NH_3SnI_3$ perovskite film where both excess SnI_2 and excess CH_3NH_3I are nearly absent. It is also interesting that portion of iodine steeply increases as the working pressure changes from 5×10^{-5} torr of 9×10^{-5} torr. The morphology of $CH_3NH_3SnI_3$ perovskite film becomes rough and many pinholes emerge in the sample as elucidated in the previous chapter. In other words, excessive CH_3NH_3I generated when depositing perovskite film in the chamber probably inhibits not only the growth of $CH_3NH_3SnI_3$ perovskite but also its crystallization.

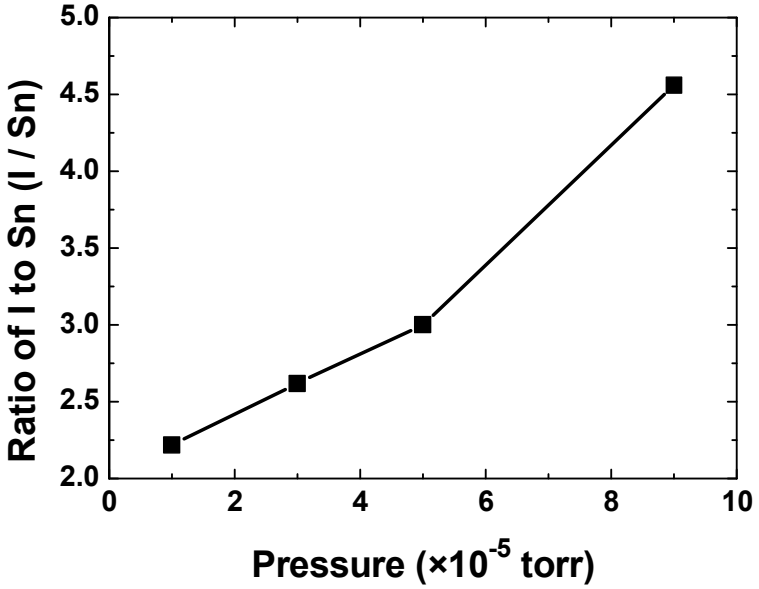

Pressure (torr)	Sn (at %)	I (at %)	Ratio (I / Sn)
1×10^{-5}	31.1	68.9	2.22
3×10^{-5}	27.6	72.4	2.62
5×10^{-5}	24.9	75.1	3.00
9×10^{-5}	18.0	82.0	4.56

Figure 3.4. Energy-dispersive X-ray spectroscopy (EDS) result of $CH_3NH_3SnI_3$ films on ITO (150 nm)/MoO_3 (5 nm)/NPB (20 nm) deposited at different pressures. Thickness of perovskite films is 122 nm, 143 nm, 180 nm and 198 nm at 1×10^{-5} torr, 3×10^{-5} torr, 5×10^{-5} torr and 9×10^{-5} torr, respectively.

3.5 Eletrical properties of perovskite film

Figure 3.5 (b) shows the electronic band gap of $CH_3NH_3SnI_3$ perovskite calculated by using Tauc plot the absorption spectrum of figure 3.5 (a). Tauc equation is written as

$$(\alpha h\nu)^2 = A(h\nu - E_g) \quad (3.2)$$

where α is absorption coefficient, h is Planck constant, ν is the frequency of photon, A is constant and E_g is the band gap energy. Absorption spectrum of the ITO (150 nm)/MoO_3 (5 nm)/NPB (20 nm)/$CH_3NH_3SnI_3$ (180 nm) sample fabricated at 5×10^{-5} torr is used for the calculation because $CH_3NH_3SnI_3$ perovskite is well formed on MoO_3/NPB interfacial layer and unreacted CH_3NH_3I (or SnI_2) is absent at working pressure of 5×10^{-5} torr as discussed previously. Electronic band gap of $CH_3NH_3SnI_3$ perovskite is found to be ~1.33 eV by Tauc plot which corresponds to the several reported ones [7]. The band gap energies of $CH_3NH_3SnI_3$ perovskite previously reported in other papers are summarized in Table 3.2. It becomes more obvious that $CH_3NH_3SnI_3$ perovskite is successfully formed and grown on MoO_3/NPB interfacial layer in vacuum process along with XRD pattern. After identifying the successful formation of perovskite, hole-only devices are fabricated to measure hole mobility of perovskite. The charge carrier mobility can be obtained by Mott–Gurney law in space

charge limited current (SCLC) region. The equation is described as

$$J = \frac{9\varepsilon\varepsilon_0\mu_0}{8}\frac{V^2}{d^3}\exp\left(\gamma\sqrt{V/d}\right) \tag{3.3}$$

where ε is dielectric constant of the material, ε_0 is permittivity in vacuum, μ_0 is zero field mobility of charge carrier, d is the distance between the electrodes and γ is the field effect mobility coefficient. The results are displayed in figure 3.6. Hole mobility for $CH_3NH_3SnI_3$ perovskite fabricated at 5×10^{-5} torr is remarkably higher than the other samples because improved crystallinity of perovskite film results in the increased charge carrier mobility [31]. It can be predicted that other electrical properties of this perovskite film will be also most improved, which is a great help to enhancing the photovoltaic performance.

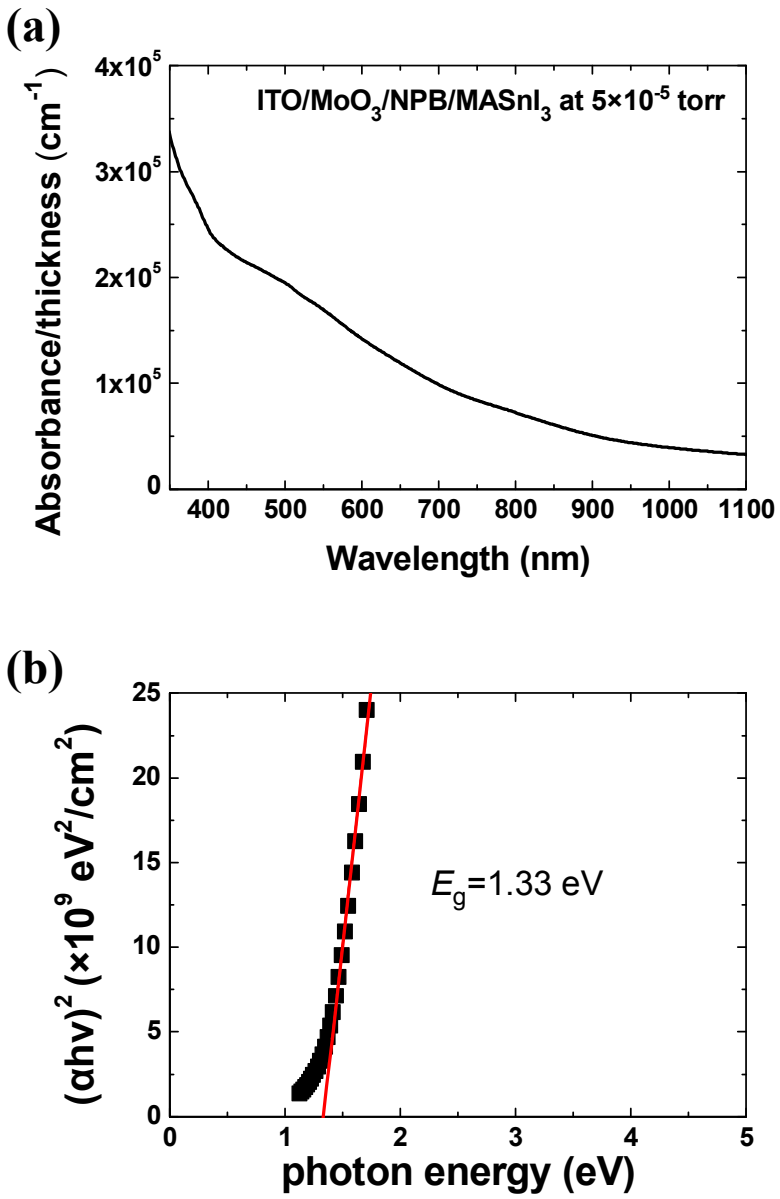

Figure 3.5. (a) The absorption spectrum of ITO (150 nm)/MoO_3 (5 nm)/NPB (20 nm)/$CH_3NH_3SnI_3$ (180 nm) sample fabricated at 5×10^{-5} torr and (b) Tauc plot obtained from the absorption spectrum

Years	Paper	Band gap	Method
2013	Tamo tsuInabe, Journal of Solid State Chemistry 205, 2013, 39–43	1.3 eV	Reflectance
2014	Mercouri G. Kanatzidis, Nature Photonics 8, 489–494 (2014)	1.3 eV	Absorption
2014	Henry J. Snaith, Energy Environ. Sci., 2014, 7, 3061-3068	1.23 eV	Absorption
2014	Kesong Yang, J. Phys. Chem. C, 2014, 118, 24383−24388	1.3 eV	DFT calculation
2015	Mercouri G. Kanatzidis, J. Am. Chem. Soc. 2015, 137, 11445−11452	1.3 eV	Reflectance

Table 3.2 Reported band gap energy of $CH_3NH_3SnI_3$ perovskite in other papers.

(a)

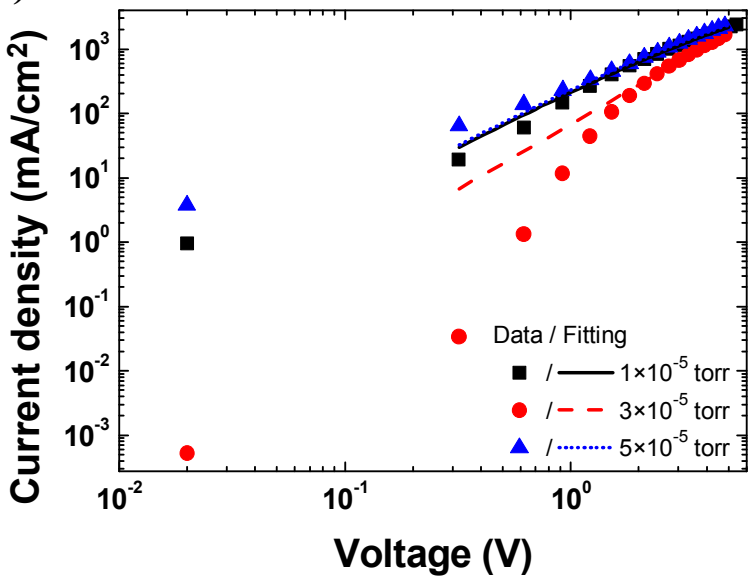

(b)

Pressure (torr)	Hole mobility ($cm^2/V \cdot sec$)
1×10^{-5}	1.72×10^{-2}
3×10^{-5}	3.53×10^{-3}
5×10^{-5}	4.02×10^{-2}

Figure 3.6. (a) The dark current curve of hole-only devices fabricated at different working pressure and (b) hole mobility calculated by the fitting in space charge limited current (SCLC) region. Thickness of perovskite films is 122 nm, 143 nm and 180 nm at 1×10^{-5} torr, 3×10^{-5} torr and 5×10^{-5} torr, respectively. The structure of hole-only device is ITO (150 nm)/MoO_3 (5 nm)/ NPB (20 nm)/$CH_3NH_3SnI_3$/MoO_3 (10nm)/Al (100 nm)

3.6 Conclusion

In this chapter, the optimal working pressure where grown $CH_3NH_3SnI_3$ perovskite has compact and crystalline morphology, stoichiometric composition and the most improved electrical properties is investigated. XRD patterns of $CH_3NH_3SnI_3$ film on MoO_3/NPB layer indicate that the crystallinity of perovskite is dramatically enhanced at 5×10^{-5} torr. It is clearly shown by SEM and AFM image that $CH_3NH_3SnI_3$ film has dense and largely crystalline morphology when fabricated at the apparent working pressure of 5×10^{-5} torr. EDS data also stands for stoichiometric perovskite film at this pressure. Electrical characteristics of perovskite is found to be consistent with the reported ones and hole mobility becomes the most improved at 5×10^{-5} torr. In summary, the apparent working pressure of 5×10^{-5} torr is the best growth condition for $CH_3NH_3SnI_3$ film on MoO_3/NPB interfacial layer.

Chapter 4

Characterization of $CH_3NH_3SnI_3$ perovskite film with various thickness

4.1 Introduction

To achieve planar lead-free perovskite solar cells, it is essential to deposit a few hundred nanometers of $CH_3NH_3SnI_3$ perovskite film for enough absorption of the sunlight. In addition, precise control over the thickness of perovskite film is a very important engineering issue to optimizing real devices. T. L. Kelly and his coworker found that the relative amount of unreacted PbI_2, light absorption and individual nano-crystalline size of perovskite gradually increases as the perovskite thickness gets larger [15]. They also revealed that device with 330 nm-thick perovskite film shows the most improved *PCE* of 11.8 %, which results from optimization of the perovskite film thickness in regard to trade-off between light harvesting efficiency and carrier diffusion lengths in $CH_3NH_3PbI_3$. Therefore, in this chapter, the effect of the $CH_3NH_3SnI_3$ perovskite thickness on absorption, film structure and overall composition will be investigated.

4.2 XRD and absorption spectrum

Figure 4.1 (a) shows the XRD pattern of $CH_3NH_3SnI_3$ perovskite film deposited on MoO_3 (5 nm)/NPB (20 nm) sublayers at 5×10^{-5} torr with changing thickness of perovskite. Every XRD pattern of perovskite shows strong and sharp peaks of (100) and (200) grains, however, the crystallinity of perovskite changes only slightly with thickness. The variation of XRD peak intensity with thickness is more exactly displayed in figure 4.2. Peak intensities of (100) and (200) perovskite grains are both increased as perovskite gets thicker, however, the increase is not that significant. This means that structure of film and morphology are hardly changing as though perovskite film is more thickly deposited in vacuum process. Also, figure 4.1. (b) indicates that the absorbance of $CH_3NH_3SnI_3$ perovskite film also increases as perovskite gets thicker, which is essential for absorbing enough light and generating more photocurrent in planar-structured perovskite solar cells.

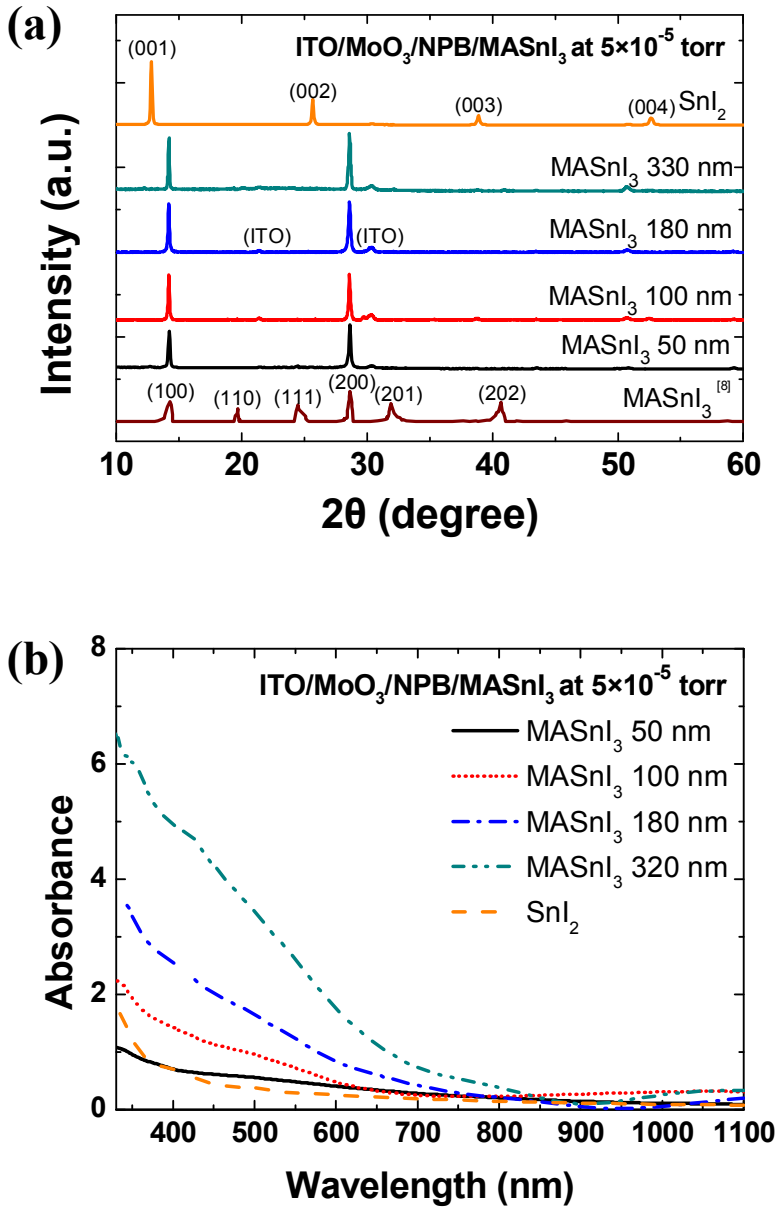

Figure 4.1. (a) The XRD pattern and (b) absorbance of ITO (150 nm)/MoO_3 (5 nm)/NPB (20 nm)/$CH_3NH_3SnI_3$ sample fabricated at 5× 10^{-5} torr with different thickness. The reported XRD pattern with peak index is powder XRD. Peak intensity of SnI_2 film is reduced by 2.5

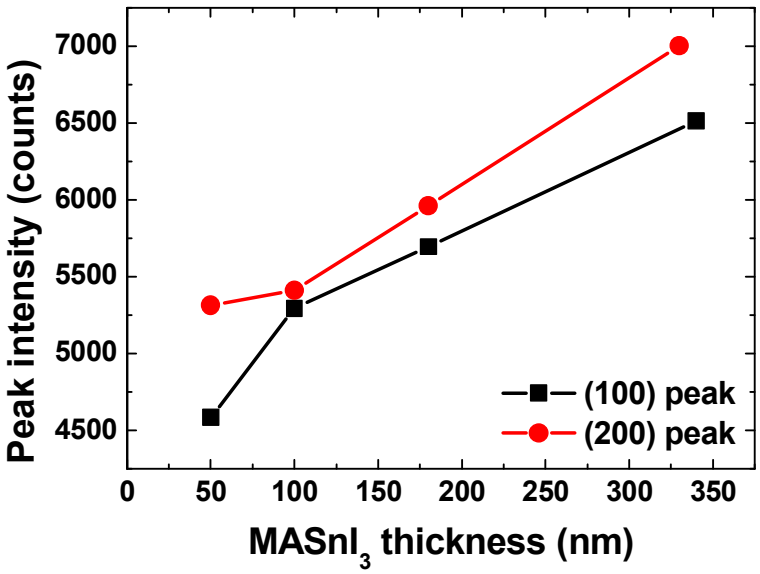

Figure 4.2. The peak intensity change of each oriented grain with thickness. The sample is ITO (150 nm)/MoO_3 (5 nm)/NPB (20 nm)/$CH_3NH_3SnI_3$ fabricated at 5×10^{-5} torr. $MASnI_3$ thickness means the thickness of $CH_3NH_3SnI_3$ perovskite film on ITO/MoO_3/NPB layer.

4.3 Cross-sectional SEM and EDS

Figure 4.3 (b) shows the elemental mapping of Sn and I for ITO (150 nm)/MoO_3 (5 nm)/NPB (20 nm)/$CH_3NH_3SnI_3$ (320 nm) sample fabricated at 5×10^{-5} torr. It is measured by cross-sectional SEM and EDS. Note that both Sn and I are all uniformly distributed in $CH_3NH_3SnI_3$ perovskite film and much of Sn also exists in the lower ITO substrate. Cross-sectional SEM image is additionally obtained for reference as shown in figure 4.3 (a). For more quantitative analysis of elements in perovskite film, atomic ratio of Sn and I is measured by using cross-sectional EDS with measuring point changed and the results are exhibited in figure 4.4. The atomic ratio of I to Sn is in the range of 2.85–3.05 and it can be concluded that the elemental compositions are nearly uniform all over the $CH_3NH_3SnI_3$ perovskite film. It is a merit of vacuum process that controlling and maintaining the deposition rate (or working pressure) are easy. Finally, $CH_3NH_3SnI_3$ perovskite film deposited by thermal evaporation in vacuum process shows considerably uniform composition as well as enhanced crystallinity by the control of growth condition although thickness of perovskite film increases a lot.

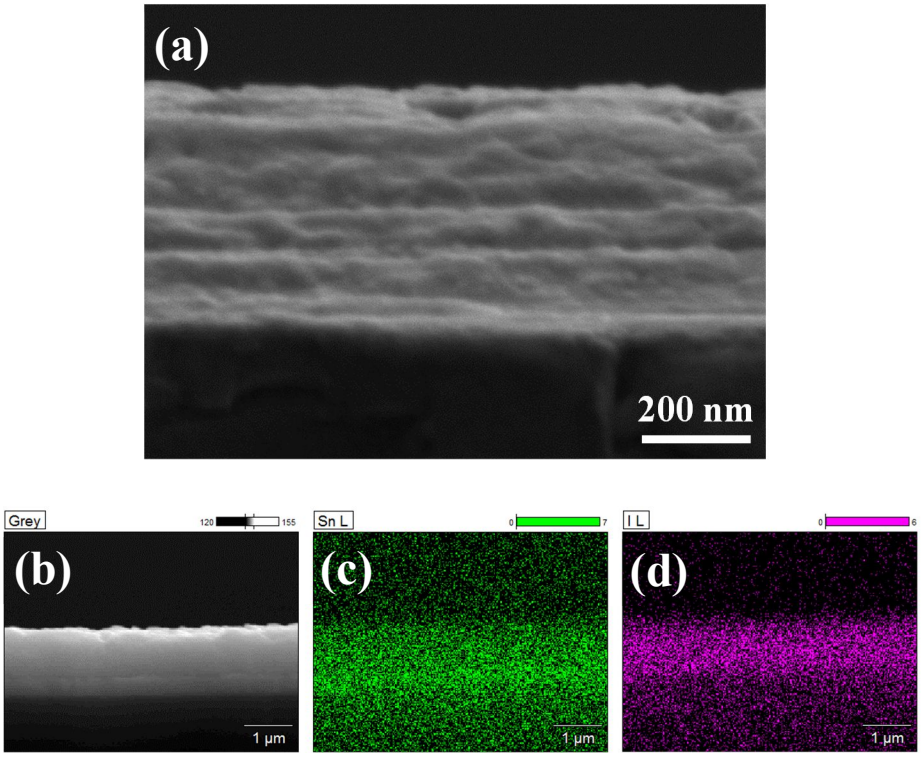

Figure 4.3. (a) Cross-sectional SEM image of ITO (150 nm)/MoO_3 (5 nm)/NPB (20 nm)/$CH_3NH_3SnI_3$ (320 nm) sample fabricated at 5×10^{-5} torr, (b) reduced image and elemental mapping for (c) Sn and (d) I.

(a)

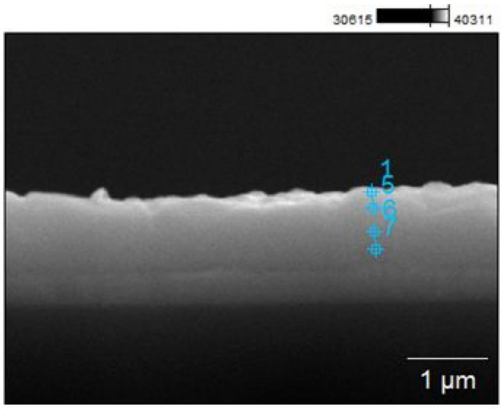

(b)

Position	Sn (at %)	I (at %)	Ratio (I / Sn)
Point 1	25.1	74.9	2.98
Point 5	24.8	75.2	3.03
Point 6	25.7	74.3	2.89
Point 7	25.9	74.1	2.86

(c)

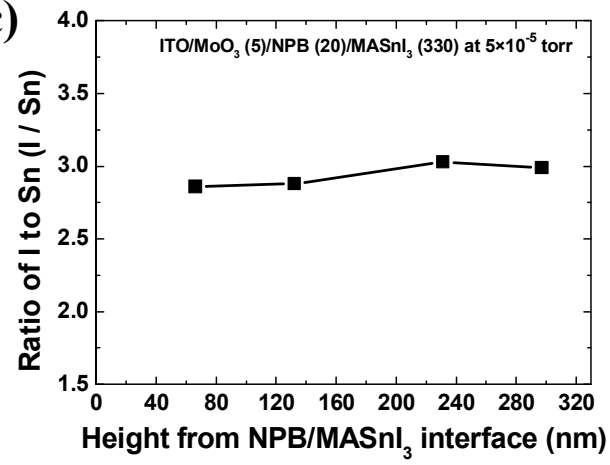

Figure 4.4. (a) Detecting image for cross-sectional EDS, (b) EDS data for each position and (c) plot of EDS results with the position. The sample is ITO (150 nm)/MoO_3 (5 nm)/NPB (20 nm)/$CH_3NH_3SnI_3$ (320 nm) fabricated at 5×10^{-5} torr.

4.4 Conclusion

In this chapter, the effect of film thickness on the properties and stoichiometry of $CH_3NH_3SnI_3$ perovskite is studied. The XRD pattern and absorption spectrum reveal that thicker perovskite layer absorbs more light while its crystallinity changes only slightly with thickness. This result is optimistic to accomplish vacuum-processed $CH_3NH_3SnI_3$ perovskite solar cells where thickness of perovskite layer is needed to be over a few hundred nanometers for absorbing enough light. In addition, vacuum-processed $CH_3NH_3SnI_3$ perovskite film exhibits ideal and totally uniform elemental composition owing to the successful control of perovskite film growth in vacuum. The conclusion is that properties of $CH_3NH_3SnI_3$ film remain the almost same even if thickness of perovskite film gets larger. Based on the results in this chapter, optical simulation and fabrication of real device with thick $CH_3NH_3SnI_3$ film will be conducted in the next chapter.

Chapter 5

Optical simulation for $CH_3NH_3SnI_3$ perovskite solar cells and real device performance

5.1 Introduction

Sn-based perovskite solar cell has been first reported in 2014 and the *PC*E has also improved up to 6.4 % recently [7-8]. But the device efficiency of lead-free perovskite solar cell is still lower than Pb-based one. Therefore, it is needed to predict maximum *PCE* of lead-free device and analyze the reason why Sn-based perovskite solar cell shows insufficient performance. In this chapter, maximum short-circuit current (J_{SC}) of lead-free perovskite device will be calculated by using refractive index of $CH_3NH_3SnI_3$ perovskite to predict maximum *PCE* and real $CH_3NH_3SnI_3$ perovskite solar cells is to be fabricated in vacuum process on the basis of optical simulation results.

5.2 Optical simulation

Figure 5.1 shows the fitting results of absorption spectrum for fused

silica/MoO_3 (5 nm)/NPB (20 nm)/$CH_3NH_3SnI_3$ samples fabricated at different working pressures. Only the sample at 5×10^{-5} torr exhibits well-fitted result, which is probably because unreacted CH_3NH_3I or SnI_2 is absent in this sample as discussed in chapter 3.4. By fitting the absorption spectrum, the refractive index (n, k) values can be obtained only for the sample deposited at 5×10^{-5} torr and these optical constants are shown in figure 5.2. And then, theoretical short-circuit current (J_{SC}) is calculated as a function of $CH_3NH_3SnI_3$ thickness in the device depicted in figure 5.3 (a) with assumption that all absorbed photons are totally converted to charge carriers and they are extracted. According to the result of figure 5.3 (b), J_{SC} can be increased up to ~23 mA/cm^2 when thickness of perovskite reaches around 500 nm. If open-circuit voltage (V_{OC}) reaches 0.88 V which is previously reported value and fill factor (FF) attains ~0.7, the power conversion efficiency (PCE) of lead-free perovskite solar cells is expected to be ~14.2 % which is comparable to the one of Pb-based perovskite solar cells. In addition, the incident photon to converted electron ratio (IPCE) spectrum in this device is simulated as a function of perovskite thickness with the same assumption. The simulation result of IPCE spectrum is shown in figure 5.3 (a). It can be confirmed that 100 nm-thick perovskite absorbs enough light in the wavelength range of 350-700 nm and absorption of light in 700-850 nm wavelength is gradually increased as perovskite

thickness changes from 100 nm to 300 nm.

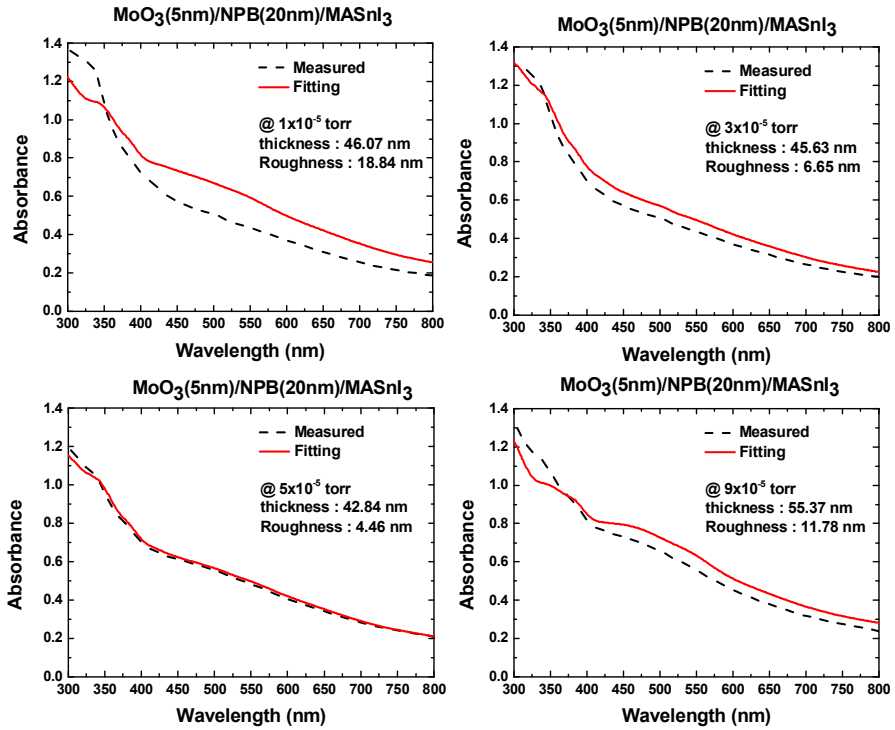

Figure 5.1. Fitting of absorption spectrum for fused silica/MoO_3 (5 nm)/NPB (20 nm)/$CH_3NH_3SnI_3$ samples fabricated at different working pressures.

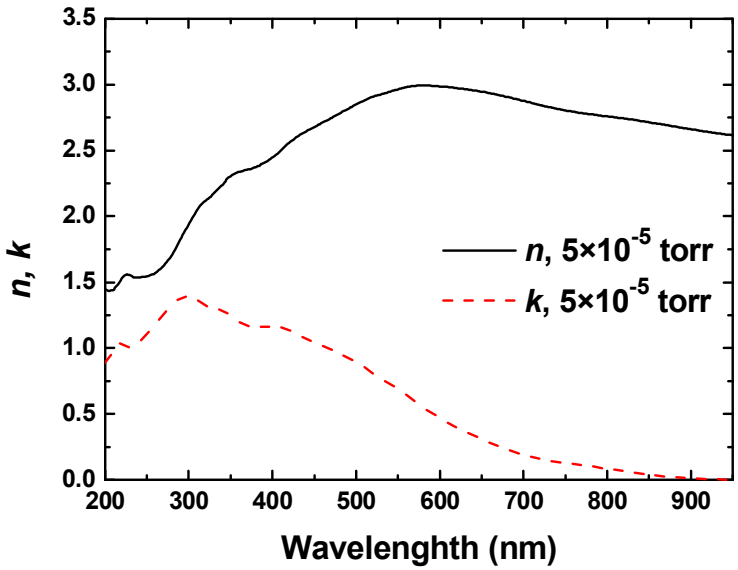

Figure 5.2. Optical constants of $CH_3NH_3SnI_3$ sample fabricated at 5×10^{-5} torr where n and k are the real and imaginary part of refractive index, respectively.

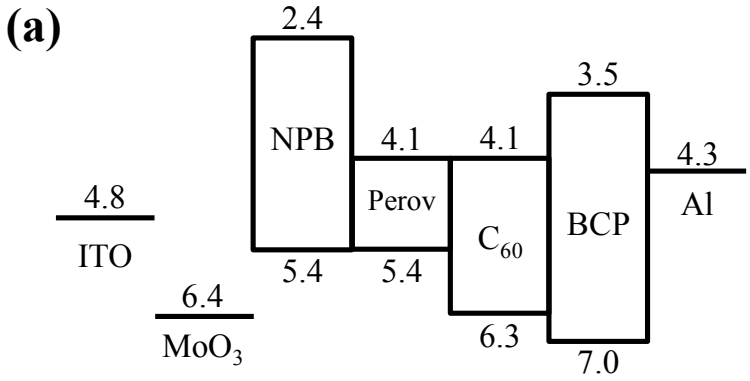
(a)
2.4
NPB
3.5
4.1
4.1
4.3
4.8
Perov
C60
BCP
Al
ITO
5.4
5.4
6.4
MoO3
6.3
7.0

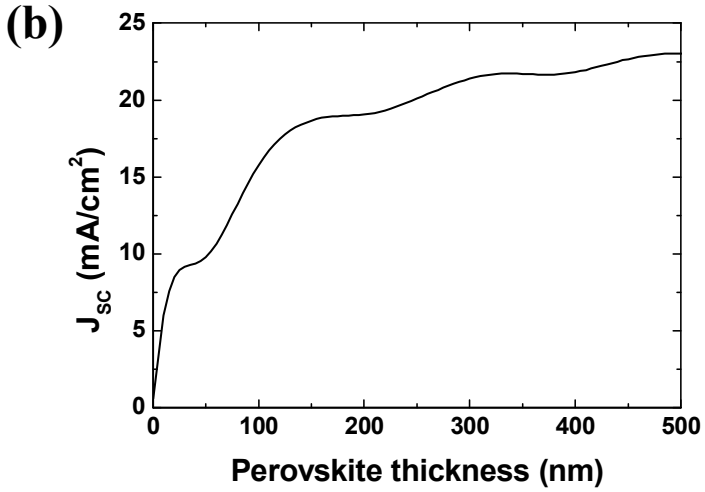
(b)
25
20
15
10
5
0
Jsc (mA/cm2)
0
100
200
300
400
500
Perovskite thickness (nm)

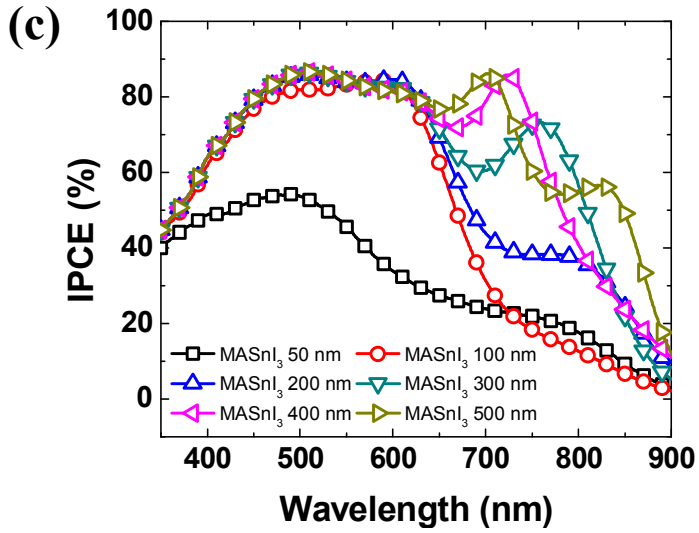
(c)
100
80
60
40
20
0
IPCE (%)
MASnI3 50 nm
MASnI3 100 nm
MASnI3 200 nm
MASnI3 300 nm
MASnI3 400 nm
MASnI3 500 nm
400
500
600
700
800
900
Wavelength (nm)

Figure 5.3. (a) Device structure used in optical simulation, (b) simulated short-circuit current (J_{SC}) and (c) incident photon to converted electron ratio (IPCE) spectrum in the device by using the refractive index of $CH_3NH_3SnI_3$ perovskite deposited at 5×10^{-5} torr.

5.3 Real device performance

Figure 5.4 shows the performance of real device whose structure is described in figure 5.3 (a). Unlike the result of optical simulation, all of the real devices exhibit poor performance. Every $CH_3NH_3SnI_3$ perovskite solar cell shows *PCE* of ~0.1 %, which mainly stems from extremely low J_{SC} which is under 5 % of simulated value as well as low *FF* regardless of perovskite thickness as shown in table 5.1. The reason for this is unclear now, however, it is probably because optimization of device is insufficient in the current state or some electrical defects interrupt the operation of lead-free perovskite solar cells.

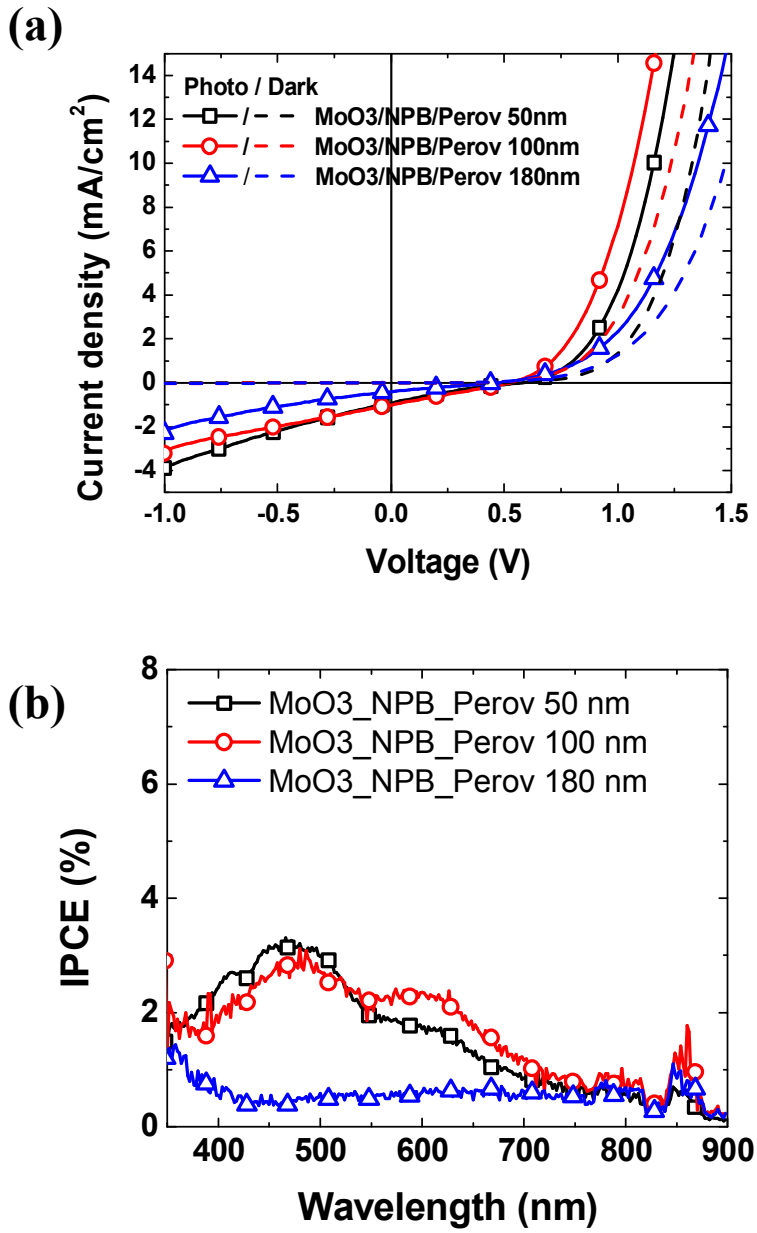

Figure 5.4. (a) J-V characteristics and (b) IPCE spectrum of the real lead-free perovskite solar device

Perovskite thickness (nm)	J_{SC} (mA/cm^2)	V_{OC} (V)	*FF*	*PCE* (%)	$J_{SC,\ int}$ (mA/cm^2)
50	0.92	0.56	0.20	0.11	0.49
100	1.01	0.53	0.25	0.13	0.55
180	0.41	0.47	0.23	0.05	0.19

Table 5.1. Table of device performance with changing $CH_3NH_3SnI_3$ thickness. $J_{SC,\ int}$ is short-circuit current calculated by using IPCE spectrum.

5.4 Discussion and conclusion

In this chapter, refractive index of $CH_3NH_3SnI_3$ perovskite is obtained from absorption spectrum to conduct optical simulation. We can obtain optical constants (n, k) of only one sample fabricated at 5×10^{-5} torr since complete and stable perovskite is formed in this condition. Optical simulation result reveals that J_{SC} is able to reach ~23 mA/cm^2 and maximum *PCE* of lead-free perovskite solar cells fabricated in vacuum process is to be over 14 %. To the best of our knowledge, this is first prediction for efficiency limit of lead-free perovskite solar cells calculated by using refractive index. Unfortunately, real device shows poor performance contrary to the simulation result. The reason is ambiguous, however, it is probably due to insufficient optimization of real device, certain electrical defects, or short carrier diffusion length reported. If optimization of $CH_3NH_3SnI_3$ perovskite solar cells and factors that limit device performance are to be verified, the efficiency of lead-free perovskite solar cells will shortly come close to the Pb-based perovskite solar cells.

Bibliography

1. V. D'Innocenzo, G. Grancini, M. J. P. Alcocer, A. R. S. Kandada, S. D. Stranks, M. M. Lee, G. Lanzani, H. J. Snaith, A. Petrozza, Nature Comm. (2014) 5, 3586.
2. H. Wang, L. Whittaker-Brooks, and Graham R. Fleming, J. Phys. Chem. C, (2015) 119, 19590−19595
3. C. Wehrenfennig, G. E. Eperon, M. B. Johnston, H. J. Snaith and L. M. Herz, Adv. Mater, (2013) 26, 1584–1589.
4. A. Kojima, K. Teshima, Y. Shirai and T. Miyasaka, J. Am. Chem. Soc. (2009) 131, 6050.
5. W. S. Yang, J. H. Noh, N. J. Jeon, Y. C. Kim, S. Ryu, J. Seo, S. I. Seok, Science (2015) 348, 1234.
6. Stoumpos, C. C., Malliakas, C. D.; Kanatzidis, M. G. Inorg. Chem. (2013) 52, 9019.
7. Hao, F.; Stoumpos, C. C.; Cao, D. H.; Chang, R. P. H.;Kanatzidis, M. G. Nat. Photonics (2014), 8, 489.
8. Noel, N. K.; Stranks, S. D.; Abate, A.; Wehrenfennig, C.;Guarnera, S.; Haghighirad, A. A.; Sadhanala, A.; Eperon, G. E.; Pathak, S. K.; Johnston, M. B.; Petrozza, A.; Herz, L. M.; Snaith, H. J. Energy Environ. Sci. (2014), 7, 3061-3068
9. Hao, F., Stoumpos, C. C., Guo, P., Zhou, N., Marks, T. J., Chang, R. P., & Kanatzidis, M. G., J. Am. Chem. Soc (2015), 137(35),

11445-11452

10. K. Zhao, R. Munir, B. Yan, Y. Yang, T. Kim and A. Amassian, J. Mater. Chem. A, 2015, 3, 20554

11. N. J. Jeon, J. H. Noh, W. S. Yang, Y. C. Kim, S. Ryu, J. Seo, S. I. Seok Nature 517, 476–480 (2015)

12. Im, J. H., Jang, I. H., Pellet, N., Grätzel, M., & Park, N. G. Nature nanotechnology, 2014, 9(11), 927-932.

13. Song, Z., Watthage, S. C., Phillips, A. B., Tompkins, B. L., Ellingson, R. J., & Heben, M. J., Chemistry of Materials, 2015, 27 (13), pp 4612–4619

14. Tsai, H., Nie, W., Cheruku, P., Mack, N. H., Xu, P., Gupta, G., ... & Wang, H. L., Chemistry of Materials, 2015, 27(16), 5570-5576.

15. Liu, D., Gangishetty, M. K., & Kelly, T. L., Journal of Materials Chemistry A, 2014, 2(46), 19873-19881.

16. M. M. Lee, J. Teuscher, T. Miyasaka, T. N. Murakami, H. J. Snaith, Science 338 (2012) 643.

17. J. Burschka, N. Pellet, S.-J. Moon, R. Humphry-Bake, P. Gao, M. K. Nazeeruddin, M. Grätzel, Nature 499 (2013) 316.

18. M. Liu, M. B. Johnston, H. J. Snaith, Nature 501 (2013) 395.

19. N. J. Jeon, J. H. Noh, Y. C. Kim,W. S. Yang, S. Ryu, S. I. Seok, Nature Mater. 13 (2014) 897–903.

20. H. Zhou, Q. Chen, G. Li, S. Luo, T.-B Song, H.-S. D, Z. Hong, J. You, Y. Liu, Y. Yang, Science 345 (2014) 542.

21. Hao, F., Stoumpos, C. C., Chang, R. P., & Kanatzidis, M. G., Journal of the American Chemical Society, 2014, 136(22), 8094-8099.

22. O. Malinkiewicz, A. Yella, Y. H. Lee, G. M. Espallargas, M. Grätzel, M. K. Nazeeruddin, H. J. Bolink, Nat. Photonics 8 (2014) 128.

23. L. E. Polander, P. Pahner, M.Schwarze, M. Saalfrank, C. Koerner, K. Leo, APL Mater. 2 (2014) 081503.

24. C.-W. Chen, H.-W. Kang, S.-Y. Hsiao, P.-F. Yang, K.-M. Chiang, H.-W. Lin, Adv. Mater. 26 (2014) 6647–6652.

25. Eperon, G. E., Stranks, S. D., Menelaou, C., Johnston, M. B., Herz, L. M., & Snaith, H. J., Energy & Environmental Science, 2014, 7(3), 982-988.

26. Koh, T. M., Fu, K., Fang, Y., Chen, S., Sum, T. C., Mathews, N., ... & Baikie, T., The Journal of Physical Chemistry C, 2013, 118(30), 16458-16462.

27. Kumar, M. H., Dharani, S., Leong, W. L., Boix, P. P., Prabhakar, R. R., Baikie, T., ... & Graetzel, M., Advanced Materials, 2014, 26(41), 7122-7127.

28. Lee, J. W., Kim, D. H., Kim, H. S., Seo, S. W., Cho, S. M., &

Park, N. G., Advanced Energy Materials, 2015, 5(20).

29. Akkerman, Q. A., D'Innocenzo, V., Accornero, S., Scarpellini, A., Petrozza, A., Prato, M., & Manna, L., Journal of the American Chemical Society, 2015, 137(32), 10276-10281.

30. S. Colella, E. Mosconi, P. Fedeli, A. Listorti, F. Gazza, F. Orlandi, P. Ferro, T. Besagni, A. Rizzo, G. Calestani, G. Gigli, F. D. Angelis, R. Mosca, Chem. Mater. (2013) 25, 4613–4618.

31. Dong, Q., Fang, Y., Shao, Y., Mulligan, P., Qiu, J., Cao, L., & Huang, J., Science, 2015, 347(6225), 967-970.

32. Takahashi, Y., Obara, R., Lin, Z. Z., Takahashi, Y., Naito, T., Inabe, T., ... & Terakura, K., Dalton Transactions, 2011, 40(20), 5563-5568.

33. Kim, B. S., Kim, T. M., Choi, M. S., Shim, H. S., & Kim, J. J., Organic Electronics, 2015, 17, 102-106.

34. Kyaw, A. K. K., Sun, X. W., Jiang, C. Y., Lo, G. Q., Zhao, D. W., & Kwong, D. L., Appl. Phys. Lett, 2008, 93(22), 221107.

초 록

유기물/무기물 혼합 페로브스카이트 태양전지는 최근 높은 전력변환 효율을 보이며 간단한 저온 공정으로 제작 가능하기 때문에 많은 주목을 받고 있다. 그러나 현재까지 보고된 대부분의 소자는 납을 기반으로 한 페로브스카이트 태양전지로 이 태양전지는 중금속 오염, 납 중독, 납 축적과 같은 심각한 문제를 일으킬 가능성이 있다. 따라서 페로브스카이트 내의 납을 다른 원소로 대체하는 것은 페로브스카이트 태양전지 분야에서 매우 중요한 주제 중의 하나이다. 주석은 주기율표 상에서 납과 같은 14족에 해당하는 원소이며 $CH_3NH_3^+$ 이온, I^- 이온과 함께 페로브스카이트 구조를 형성한다고 알려져 있기 때문에 현재까지 주석이 납을 대체할 수 있는 가장 유력한 원소로 생각되어왔다. 이러한 지식을 바탕으로 2014년 이후 납이 없는 주석 기반 페로브스카이트 태양전지를 일부 논문에서 보고하였으나 모든 주석 기반 소자들은 용액 공정으로 제작되었다. 용액 공정에서는 페로브스카이트 아래의 전자 수송 층이 다공성 TiO_2로 제한되어 $CH_3NH_3SnI_3$ 박막의 표면 특성이 나빠지

는 문제점이 있다. 또한 용액 공정으로 제작된 $CH_3NH_3SnI_3$ 페로브스카이트 박막은 산화에 대한 안정성이 낮고 전하 확산 거리가 짧다는 것이 문제점으로 보고되었다. 따라서 진공 공정이 $CH_3NH_3SnI_3$ 페로브스카이트 박막을 증착하는데 효과적인 방법이 될 수 있다. 왜냐하면 진공 공정은 깨끗한 환경, 다양한 전하 수송 층의 선택 가능성, 높은 재현성과 같은 여러 가지 장점을 가지고 있기 때문이다. 진공 공정에서 수분 및 용매가 없는 깨끗한 증착 환경은 산화에 민감한 $CH_3NH_3SnI_3$ 박막에 매우 효과적이며, 페로브스카이트의 표면 구조와 에너지 준위를 고려하여 가장 적합한 전하 수송 층을 선택할 수 있다.

본 학위 논문에서는 다양한 정공 수송 층을 도입하여, 이 하부의 정공 수송 층이 진공 증착된 $CH_3NH_3SnI_3$ 페로브스카이트 박막의 성장에 미치는 영향을 조사하였다. 그 결과 ITO, ITO/MoO_3와 비교했을 때 ITO/MoO_3/NPB 층 위에 증착된 $CH_3NH_3SnI_3$ 페로브스카이트 박막이 가장 향상된 결정성을 나타내었다. 또한 X선 회절 분석을 통해 초기에 정공 수송 층 위에 증착되는 2 nm의 SnI_2가 최종적인 $CH_3NH_3SnI_3$의 성장 및 결정성에 직접적인 영향을 미친다는 사실을 알 수 있었다. 추가적으로 진공 챔버의 작동 압력과 박막 두께가 $CH_3NH_3SnI_3$ 페로브스카이트 박막의 성장 및 특성에 미치는

영향이 조사되었다. 승화된 CH_3NH_3I에 의해 작동 압력을 상승시켜 가며 증착한 결과, 이온 게이지에 표시되는 작동 압력이 5×10^{-5} torr일 때 화학량론적이고 결정질에 가까운 표면을 갖는 $CH_3NH_3SnI_3$ 페로브스카이트 박막이 성공적으로 형성되었다. 이 압력에서 만들어진 페로브스카이트 박막은 가장 높은 정공 이동도와 함께 1.33 eV의 밴드 갭 에너지를 나타내었다. 또한 페로브스카이트의 두께가 증가하여도 박막의 특성과 균일성에는 큰 영향을 주지 않는 것으로 확인되었다. 그리고 최종적으로 광학 시뮬레이션과 실제 $CH_3NH_3SnI_3$ 페로브스카이트 태양전지 제작을 시도하였다. 비록 실제 소자는 완전한 최적화가 되지 않아 좋지 못한 성능을 보였지만, 광학 계산 결과 페로브스카이트의 두께가 약 500 nm에 도달하였을 때 단락 전류 밀도가 최대 23 mA/cm^2까지 향상될 수 있음을 확인하였다. 만약 개방 전압과 충진율이 이전에 보고된 수준인 약 0.88 V, 0.7까지 각각 도달한다고 가정하면, 납이 없는 페로브스카이트 태양전지의 효율은 최대 14.2 %까지 향상될 것이며 납을 기반으로 한 페로브스카이트 태양전지에 버금가는 수준의 효율에 도달할 것으로 기대된다.

주요어: 유기물/무기물 혼합 페로브스카이트 태양전지, 진공

공정, 하부층, $CH_3NH_3SnI_3$, 납이 없는 페로브스카이트, MoO_3, NPB

학 번: 2014 - 21461